REPORT

All-cellulose hydrogel-based adhesive

Xia Sun,[1] Zhenqian Pang,[2] Yeling Zhu,[1] Zhengyang Yu,[1] Pu Yang,[1] Liyang Liu,[3] Scott Renneckar,[3] Teng Li,[2,*] and Feng Jiang[1,*]
*Correspondence: lit@umd.edu (T.L.); feng.jiang@ubc.ca (F.J.)
Received: August 14, 2023; Accepted: November 30, 2023; Published Online: December 2, 2023; https://doi.org/10.59717/j.xinn-mater.2023.100040

GRAPHICAL ABSTRACT

PUBLIC SUMMARY

- Dialcohol cellulose nanorods are prepared through sequential oxidation and reduction.
- Primary hydroxyl groups bring about more out-of-plane hydrogen bonds.
- Concentrated dialcohol cellulose nanorods can form an all-cellulose hydrogel.
- The all-cellulose hydrogel shows high adhesion to various substrates.

REPORT

All-cellulose hydrogel-based adhesive

Xia Sun,[1] Zhenqian Pang,[2] Yeling Zhu,[1] Zhengyang Yu,[1] Pu Yang,[1] Liyang Liu,[3] Scott Renneckar,[3] Teng Li,[2,*] and Feng Jiang[1,*]

[1]Sustainable Functional Biomaterials Laboratory, Department of Wood Science, University of British Columbia, Vancouver BC V6T 1Z4, Canada

[2]Department of Mechanical Engineering, University of Maryland College Park, College Park, Maryland 20742, USA

[3]Advanced Renewable Materials Lab, Department of Wood Science, University of British Columbia, Vancouver BC V6T 1Z4, Canada

*Correspondence: lit@umd.edu (T.L.); feng.jiang@ubc.ca (F.J.)

Received: August 14, 2023; Accepted: November 30, 2023; Published Online: December 2, 2023; https://doi.org/10.59717/j.xinn-mater.2023.100040

Citation: Sun X., Pang Z., Zhu Y., et al., (2023). All-cellulose hydrogel-based adhesive. The Innovation Materials **1(3)**, 100040.

Hydrogels showing strong adhesion to different substrates have garnered significant attention for engineering applications. However, the current development of such hydrogel-based adhesive is predominantly limited to synthetic polymers, owing to their exceptional performance and an extensive array of chemical options. To advance the development of sustainable hydrogel-based adhesives, we successfully create a highly robust all-cellulose hydrogel-based adhesive, which is composed of concentrated dialcohol cellulose nanorods (DCNRs) and relies on enhanced hydrogen bonding interactions between cellulose and the substrate. We implement a sequential oxidization-reduction process to achieve this high-performance all-cellulose hydrogel, which is realized by converting the two secondary hydroxyl groups within an anhydroglucose unit into two primary hydroxyl groups, while simultaneously linearizing the cellulose chains. Such structural and chemical modifications on cellulose chains increase out-of-plane interactions between the DCNRs hydrogel and substrate, as simulations indicate. Additionally, these modifications enhance the flexibility of the cellulose chains, which would otherwise be rigid. The resulting all-cellulose hydrogels demonstrate injectability and strong adhesion capability to a wide range of substrates, including wood, metal, glass, and plastic. This green and sustainable all-cellulose hydrogel-based adhesive holds great promise for future bio-based adhesive design.

INTRODUCTION

Nowadays, hydrogel-based adhesives have been widely explored for surface engineering, particularly for bonding a variety of substrates.[1–3] Researchers have harnessed a wide range of synthetic or natural polymers[4–6] to design hydrogel-based adhesives, leveraging interactions between the hydrogel and substrates or employing precise structural regulation techniques to achieve high bonding strength. Nonetheless, the widespread use of petroleum-based synthetic polymers, including polyethylene glycol,[7,8] polyacrylamide[9,10] and polyacrylic acid,[11–13] has raised concerns about their potential environmental and human health risks, which could impede the pursuit of carbon neutrality. Although natural polymers like tannin,[14,15] chitosan[16] or gelatin[17] have been utilized to engineer hydrogel-based adhesives, their widespread application has been limited due to either the need for a complex modification process or their inferior adhesion strength.

Cellulose, the most abundant biopolymer on Earth, has been utilized for adhesives through cellulose dissolution and regeneration processes,[18,19] or by incorporating it with other polymers.[20] However, the practical applications of these approaches are severely restricted due to the use of large amounts of solvents and additional polymers. Despite ongoing research, the development of all-cellulose-based adhesive has faced limited progress. Recently, cellulose nanocrystals (CNCs) suspension has shown promise in forming super-structured bonds through confined assembly between adherends. However, the anisotropic nature of the adhesive strength, with significantly lower strength in the out-of-plane direction compared to the in-plane direction (at least two orders of magnitudes lower), limits its potential applications.[21] Therefore, the ever-growing environmental concern and high-performance requirement call for the development of strong hydrogel-based adhesives (>2 MPa lap shear strength) derived from natural and renewable sources, particularly cellulose.

Engineering the interactions between substrate and hydrogel plays a pivotal role in the design of high-performance hydrogel-based adhesives. Currently, chemical interactions, including Schiff base reaction,[22] Michael addition reaction,[23] and EDC/NHS coupling,[11] as well as physical interactions such as electrostatic interactions,[24] hydrogen bonding,[25] and topological adhesion,[24] have been widely employed for the design of hydrogel-based adhesives. Among them, hydrogen bonding represents the most prevalent molecular interaction in nature. Despite the relatively modest bonding energies of hydrogen bonds, such as approximately 20.9 kJ/mol for N-H···O and around 29 kJ/mol for O-H···O,[26] achieving high adhesion is possible through strategies such as increasing the hydrogen-bonded cluster densities or utilizing double,[25] triple,[27] and even quadruple[28] hydrogen bonding system. For example, strong hydrogel adhesion (80 kPa toward glass) toward a range of surfaces can be enabled by incorporating "triple hydrogen bonding clusters" through a unique "load sharing" effect and an increase in bond density.[29] Also, by adjusting the hydrogen bonds in the polymer network, smart materials based on biomacromolecules can also be fabricated.[30,31] When it comes to cellulose, even though it possesses abundant hydroxyl groups that can potentially act as binding sites for hydrogen bonds, their effective utilization in the development of hydrogel-based adhesives is still challenging. This is primarily due to the rigid cellulose structures, which significantly restrict the formation of out-of-plane interactions.[32,33] Therefore, we propose that hydrogen bonds can be regulated between cellulose and substrates to form a strong hydrogel-based adhesive by converting the secondary hydroxyl groups to primary hydroxyl groups via a ring-opening reaction.

Herein, for the first time, we have developed a strong adhesive based on all-cellulose hydrogel consisting of concentrated dialcohol cellulose nanorods (DCNRs) prepared through a sequential periodate oxidization – borohydride reduction process. The periodate oxidation partially converts the anhydroglucose unit (AGU) ring structure of cellulose into a linear structure. This transformation enhances chain flexibility, facilitating the formation of mechanical interlocks. Further reducing the generated aldehyde groups into primary hydroxyls by borohydride reduction treatment is expected to contribute to the formation of more out-of-plane hydrogen bonds. Especially, the conversion from two secondary hydroxyl groups into two primary hydroxyl groups provides enhanced chain flexibility and thereby induces more out-of-plane interactions between cellulose and substrates, therefore increasing the adhesion performances. We further explored the rheological properties of the formed hydrogel and examined the adhesion strength to different substrates. More importantly, the underlying mechanisms of the adhesive were proposed and verified using spectroscopy and first-principle density functional theory (DFT) calculation. Given that the hydrogel-based adhesive consists of only DCNRs and water, this green and sustainable all-cellulose adhesive holds significant promise for large-scale production and possesses the potential to replace existing commercial fossil-based counterparts.

MATERIALS AND METHODS

Materials

Northern bleached softwood kraft pulp (NBSK) was kindly provided by Pulp and Paper Centre at University of British Columbia. Sodium metaperiodate ($NaIO_4$, 98%, Alfa Aesar), sodium chloride (NaCl, 98%, Alfa Aesar) were purchased from Fisher Scientific, USA. Sodium borohydride ($NaBH_4$ 98+%) was purchased from Acros Organics, USA. All reagents are used as received without further purification. All water used is deionized water from the Barnstead Mega-Pure System.

Synthesis of DCNRs and DCNRs hydrogel-based adhesives

Firstly, 7 g NBSK pulp was swollen in 700 mL DI water for 24 hours. Then, 9.24 g $NaIO_4$ (anhydroglucose unit (AGU): periodate = 1:1 molar ratio) and 27.09 g NaCl were added into the pulp suspension and reacted for 72 h in a

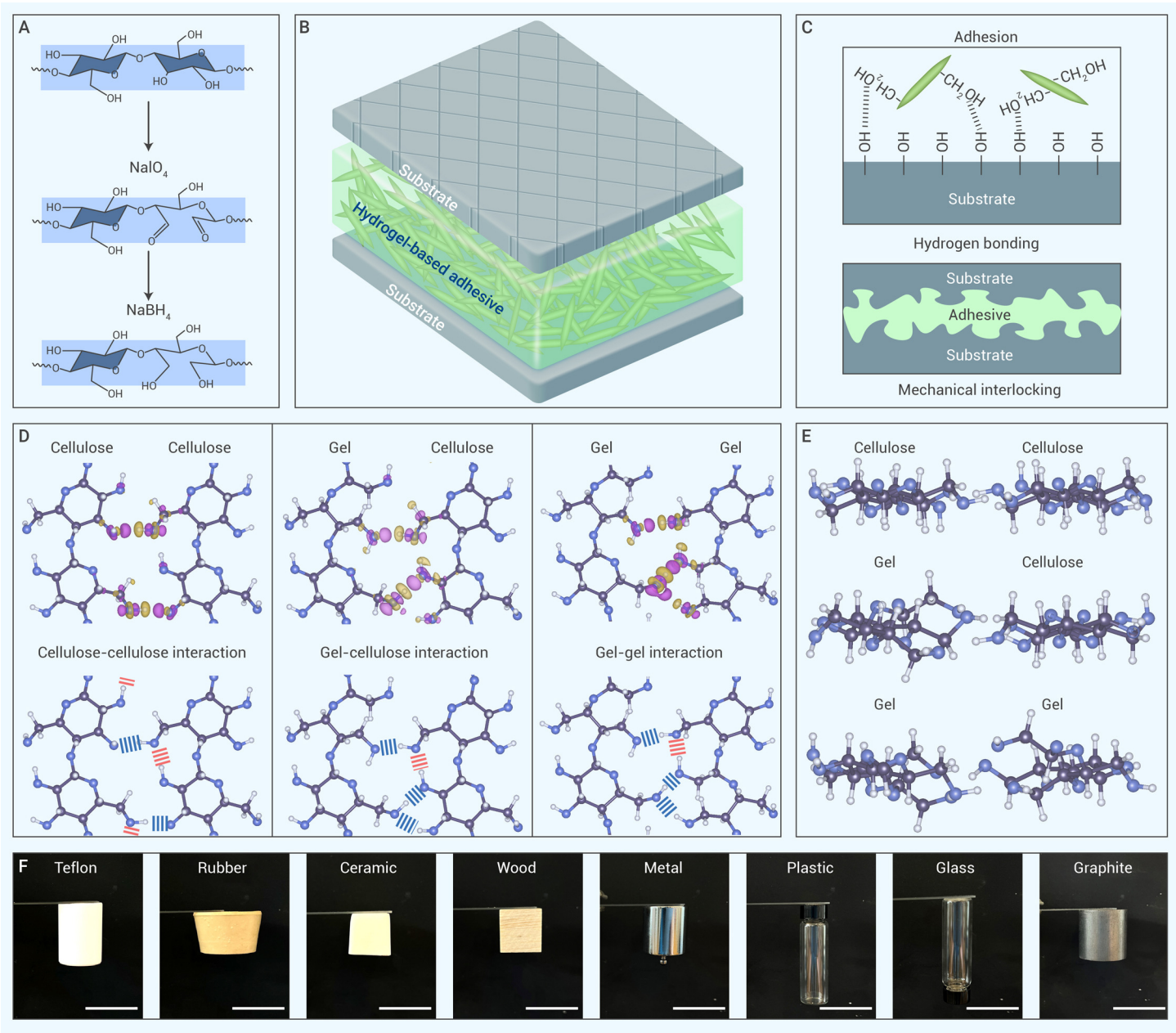

Figure 1. Schematic illustration of DCNRs hydrogel-based adhesive (A) The preparation process of DCNRs. (B) Schematic illustration of the adhesion of substrates using DCNRs hydrogel-based adhesive. (C) Schematic illustration of the adhesion mechanisms between hydrogel-based adhesive and substrates. (D) Differential charge densities (top panel) and hydrogen bonds (bottom panel) in the DFT-optimized molecular structures: cellulose-cellulose interaction, DCNRs gel-cellulose interaction, and DCNRs gel-DCNRs gel interaction. Oxygen, carbon, and hydrogen atoms are represented with blue, black, and white beads, respectively. Yellow and purple shades in the charge density represent the loss and gain of electrons, respectively. Blue and orange dashed lines in each bottom panel represent the inter- and intra-molecular hydrogen bonding, respectively. The isosurface is set as 0.003 e/Bohr^3. (E) Side view of the molecular structures in cellulose-cellulose interaction, DCNRs gel-cellulose interaction, and DCNRs gel- DCNRs gel interaction. (F) Demonstration of DCNRs hydrogel-based adhesive adheres on various substrates (Scale bar: 3 cm).

light-free environment at room temperature. After dialysis against deionized water (Spectra/Por molecularporous membrane tubing with molecular weight cut-off value of 12-14 kDa) for 1 week, 3.5 g $NaBH_4$ was added in the collected suspension and reacted for 24 h to reduce the aldehyde groups. The suspension was dialyzed against DI water for another week. After dialysis, the suspension was frozen in a freezer under -20°C, then lyophilized through a freeze-dryer for 4 days and then collected for future use.

The DCNRs hydrogel-based adhesive was prepared by dispersing the lyophilized DCNRs in DI water at varied concentrations of 15, 20, 25, and 30 wt% (shorted as H-x, where x represents the DCNRs concentration). To ensure complete dispersion, the suspension was bath sonicated for 1 hour in a sonication bath and then placed at 4°C for future use.

Characterizations of DCNRs

For nuclear magnetic resonance (NMR) tests, 5 mg dried DCNRs were dispersed into 50 mL DMSO-d6 (Sigma Aldrich) and transferred into 5 mm NMR tubes. ^{1}H and ^{13}C NMR spectra were recorded on a Bruker Avance 300 MHz spectrometer (Bruker, Switzerland) with a 5 mm broadband observe (BBO) probe. Proton spectra were obtained at 298.15 K with the zg pulse program, 90° pulse width, scanning number 256, delay time 1 s, and acquisition time 5.6 s. The inverse-gated proton decoupling pulse program (*zgig*) was applied to receive the carbon spectra at 298.15 K with scanning number 20000, delay time 2 s, 90° pulse width, and acquisition time 1.4 s. The topspin 3.6 software was applied to convert the received FID signals to NMR spectra by the Fourier transform, phase change, baseline correction, and calibration using the solvent peak (δH/δC=2.5 ppm/ 39.5 ppm). ^{13}C CP-MAS NMR spectra with high power proton decoupling were collected on a 400MHz Bruker solid-state widebore AVANCE spectrometer. Samples were first milled into powders and then spined at 6kHz at magical angle. ^{13}C pulse with a ramped amplitude at 50% was used for cross polarization with a contact time of 5

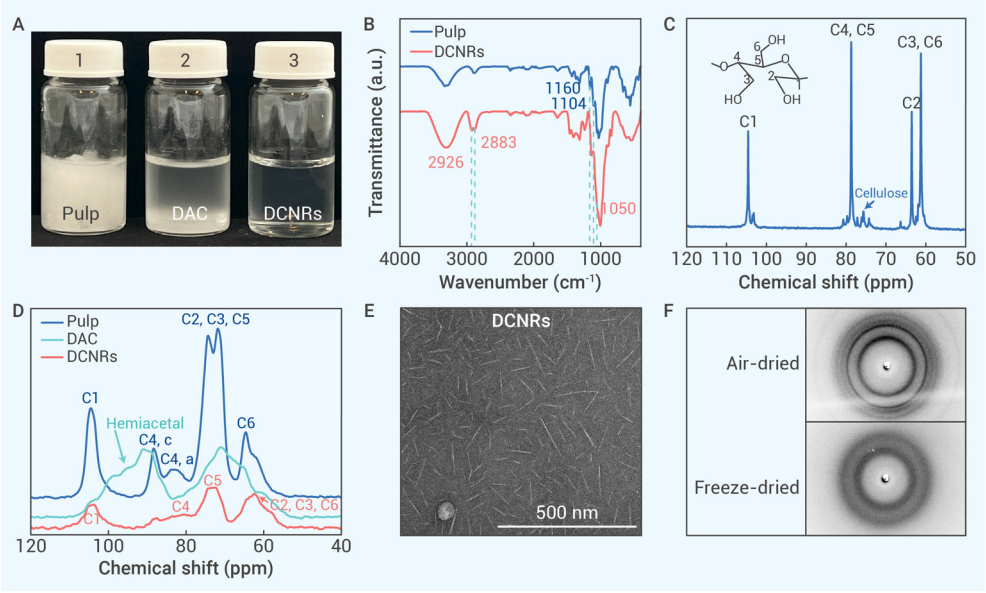

Figure 2. Characterizations of DCNRs (A) Digital photos of 1 wt% (1) pulp suspension and after (2) oxidization and (3) reduction. (B) ATR-FTIR spectra of pulp and DCNRs. (C) ^{13}C NMR spectra of DCNRs. (D) ^{13}C CP-MAS NMR of original pulp, DAC, and DCNRs. (E) TEM image of DCNRs. XRD pattern of (F) DCNRs film under ambient drying and freeze-dried sample.

ms. The relaxation delay was 5 seconds, and the acquisition time was 50 ms. Data was processed with a 50Hz line broadening exponential decay function before Fourier Transform. Chemical shift values (ppm) were referenced with adamantane before data acquisition. All experiments were done at room temperature.

Other characterizations of DCNRs were mentioned in the supporting information.

Rheology tests

Viscoelastic properties of DCNRs hydrogels with different concentrations were studied by a rheometer (AR2000, USA). For stress sweep, the stress range was from 0.01-500 Pa for 20%, 25%, and 30%, 0.01-100 Pa for 15%, and the angular frequency was all fixed at 1 Hz. For strain sweep, the strain range was 0.1-100% and the angular frequency was all fixed at 1 Hz. For the frequency sweep, the frequency range was 0.1-50 Hz and the oscillation stress was fixed at 0.1768 Pa. The shear rate range for viscosity measurement was from 0.1-10 1/s.

Adhesive tests

Adhesion strength was measured through lap shear tests via a materials testing system (Instron 5969). Different substrates (basswood, Douglas fir wood, copper, plastic, aluminum, and glass) were firstly prepared into rectangular slides (width: ~2 cm, length: ~8 cm) A specific weight of DCNRs hydrogel-based adhesives was injected onto one sample slide and overlapped by another sample (overlapped area, S: ~4 cm^2). After curing for 3 days at room temperature, the samples were tested on the Instron machine with a crosshead speed of 1.5 mm/min and a load cell of 2000 N. The adhesion strength was calculated by F/S, where F was the maximum stretch force and S was the overlapped area.

Simulation procedures

First-principle density-functional theory (DFT) calculations are performed using the Vienna Ab initio Simulation Package (VASP)[34,35]. The projector augmented wave (PAW) pseudopotentials[36] and the generalized gradient approximation (GGA) of the Perdew-Burke-Ernzerhof (PBE) functional[37] are used. A plane-wave basis is set with a kinetic-energy cut-off of 500 eV. The Monkhorst-Pack[38] k-point mesh of is used for structure optimization and electronic calculations of the system. Periodic boundary conditions are applied in the x-, y- and z-directions for all calculations, while a large vacuum space (15 Å) is added in the z-direction to avoid interactions between periodic images of cellulose and gel chains. To consider the effects of van der Waals interactions (VDW), the DFT-D2 method of Grimm[39] is incorporated in all the calculations. All structures are relaxed using a conjugate gradient algorithm until the atomic forces are converged to 0.01eV/Å.

In the electronic calculation, the differential charge density is defined as $\Delta\rho=\rho_{total}-\rho_{chain1}-\rho_{chain2}$, where is the fully-optimized total charge density of the system. To obtain and , a single point calculation of the charge density is performed on each chain, which is extracted from the system and isolated into a separate box. The same calculation method is also utilized in the following analysis of the total energy of the system and the individual energy of each chain.

Characterizations of DCNRs

Attenuated total reflectance-FTIR (ATR-FTIR) was tested on INVENIO S (Bruker Optics Pty. Ltd., Billerica, MA, USA) with a diamond crystal at a resolution of 4 cm^{-1} in the range of 4000-400 cm^{-1} for original NBSK pulp and obtained DCNRs in the form of thin films. The morphology of DCNRs was observed through Transmission Electron Microscope (TEM, Tecnai Spirit) and Atom Force Microscopy (AFM). For TEM, 0.01 wt% DCNRs on a glow-discharged formvar-carbon copper grid was negatively stained with 2% uranyl acetate and then observed under 120 kV accelerating voltage. The size of DCNRs was estimated through Nano Measurer 1.2. For AFM, a single droplet of 0.0002 wt% suspension was deposited and dried on a freshly-peeled mica surface. The sample was then imaged using a Bruker MultiMode-8 AFM (Bruker, Billerica, MA, USA) equipped with a J-scanner. The height profiles were captured using an Al-coated, Sb-doped Si cantilever (Bruker VTESPA-300, Billerica, MA, USA) with 40 N/m in spring constant and 300 kHz as resonance frequency, in the peak force tapping mode. Nanoscope Analysis software was employed to process the height profiles into 2D images at the dimensions of 5 × 5 μm^2. The height distribution profile was obtained based on over 100 individual nanoparticles.

XRD diffractogram of NBSK pulp, dialdehyde cellulose (DAC) and DCNRs was obtained through a Bruker D8-Advance X-ray diffractometer (Bruker, Germany) equipped with Cobalt radiation (40 kV and 50 mA) at a scanning speed of 1° min^{-1} from 2q = 5–55°. The samples in sheet forms were pressed between two edges of 1 mm-thick flat plate and cut by a sharp blade to prepare a block in which the sheets are stuck perpendicular to the flat surface. The sample was mounted on a sample holder with a collimator so that the incident X-ray beam would be parallel to the constituent sheets. Powder samples were mounted on a 1 mm thick perforated disk with a Mylar window. Imaging plate (10 cm x 8 cm) was positioned at 5 cm from the sample using a cassette, and exposure was done in a vacuum box connected to an X-ray generator (Philips PW3830) with a Cu X-ray tube operated at 30 kV and 20 mA. The incident beam was filtered with Ni foil to reduce the Kβ line. Typical exposure time was 1 hour, and the image plate was scanned using image-late reader (BAS-1800 II, Fujifilm). The readout values were converted to numbers proportional to photon counts for presentation.

Differential scanning calorimetry (DSC) measurements were conducted on a TA Q1000 calorimeter (TA instruments, USA) using the following procedure. Firstly, the sample was cooled to 0 °C at a rate of 10 °C/min and kept for 2 min. Secondly, the sample was heated to 200 °C at a rate of 10 °C/min, and the sample was then cooled to 0 °C and heated to 200°C at a rate of 10 °C/min.

The aldehyde content was determined by titration. Firstly, ~100 ml (dry mass~0.1 g) dialdehyde cellulose was adjusted to pH=3 by 0.1 mol/L HCl. Then, hydroxylamine hydrochloride was added into the solution and reacted for 2 h. Then, the solution was titrated by 0.1 mol/L NaOH to pH=3. The aldehyde content was calculated as: c(NaOH)*v(NaOH)/m(DAC).

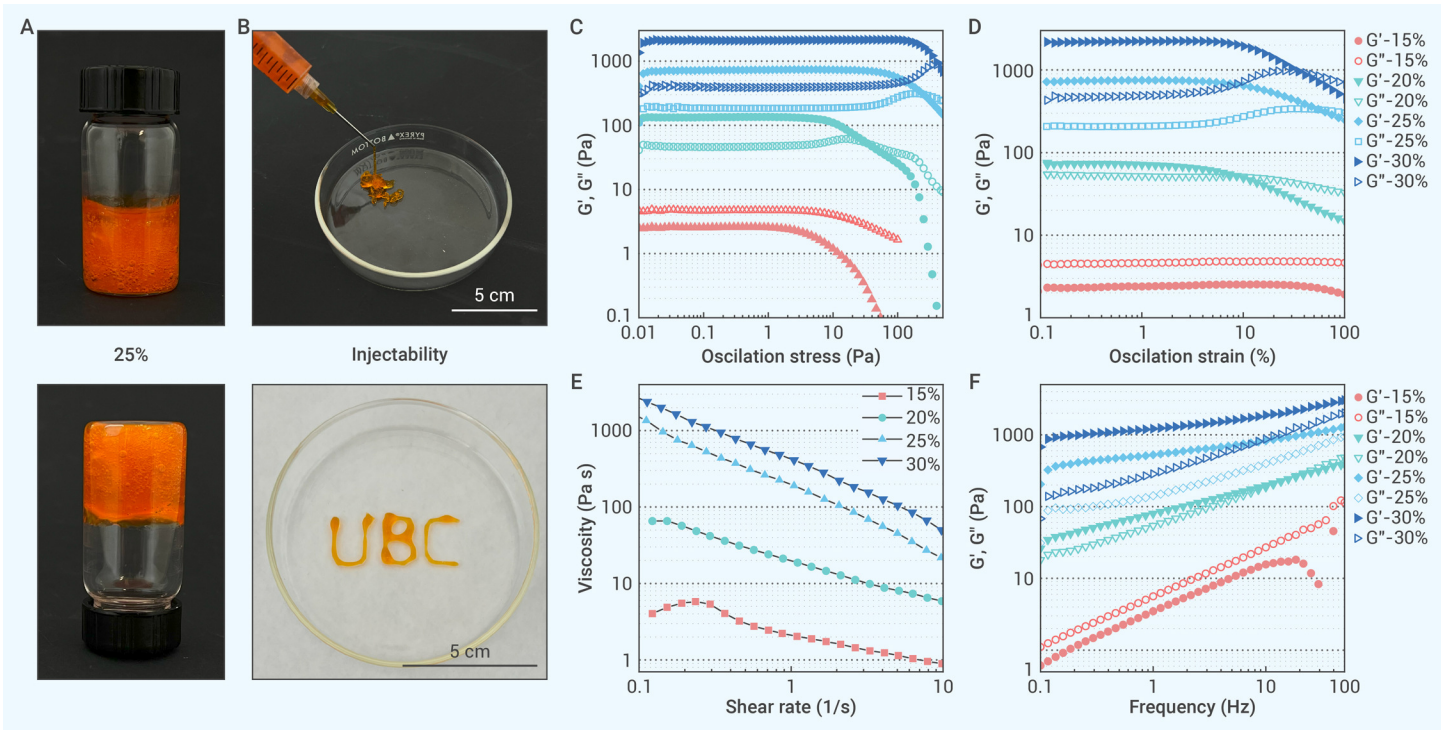

Figure 3. Injectability and rheological property of DCNRs hydrogels (A) Digital photo of H-25% showing stable gel-like behavior (the gel was dyed with Rhodamine B for better visualization); (B) Demonstration of injectability of H-25% (scale bar: 5 cm). (C) Stress sweep and (D) strain sweep of DCNRs-based hydrogel with different concentrations. (E) Apparent viscosity of different DCNRs hydrogels under steady shear from 0.1 s^{-1} to 10 s^{-1} at 25°C. (F) Frequency sweep of DCNRs hydrogels with different concentrations.

RESULTS AND DISCUSSION

Design concept of all-cellulose hydrogel-based adhesive

Although cellulose is considered as the most abundant polymer on Earth, the development of all-cellulose based adhesives has been limited. Due to the nano-scaled dimension and abundant surface hydroxyl groups, nanocellulose is known to form strong cohesive bonds to yield super-strong film (>100 MPa) upon drying.[40-44] However, cellulose generally does not show satisfactory adhesive strength to bind different substrates together. According to the adhesion theory, where both physical and chemical interactions are needed to form strong cohesive and adhesive bonds, it is hypothesized that the weak adhesive strength of cellulose could be ascribed to the low flexibility and mobility of cellulose chains caused by the rigid AGU rings and restricted rotation due to the intramolecular hydrogen bonds (O3H···O5, O2H···O6).[45] Such low flexibility and mobility of cellulose chains can restrict the diffusion of cellulose into the substrate to form strong chemical and physical interactions. Therefore, we proposed a two-step ring opening–reduction strategy to synthesize all-cellulose adhesive. Firstly, as the AGU contains vicinal diols at the C2 and C3 positions, which can be selectively cleaved through periodate oxidation (Figure 1A), the ring structure can be opened to enhance the chain flexibility. Secondly, the aldehyde groups generated by periodate oxidation will be further reduced into primary hydroxyl groups and produce dialcohol cellulose nanorods (DCNRs). Compared to the secondary hydroxyl groups fixed on the rigid AGU rings, the two primary hydroxyl groups linked on the linear AGU chains exhibit more flexibility for hydrogen bonding and mechanical interlocking with the adherend. Through this sequential oxidation-reduction reaction, we speculate that DCNRs hydrogel-based adhesive (Figure 1B) can be realized due to the enhanced chain flexibility and hydrogen bonding density.

As both cohesion and adhesion are critical for high-performance adhesive, Figure 1C schematically illustrates the adhesion of DCNRs hydrogel in the bonding process. For adhesion, the breakage of AGU rings generates two primary hydroxyl groups on the DCNRs surface. Therefore, the abundant hydroxyl groups on the flexible surface chains will interact with substrates through hydrogen bonds, while the flexible cellulose chains on the DCNRs will form mechanical interlocking with substrates, resulting in a high adhesion performance. For cohesion, the ring-opening of AGU reduces the steric effect and thereby induces more intermolecular hydrogen bonds between DCNRs. The cohesive force of DCNRs was assessed by measuring the tensile strength of a dried DCNRs film, which demonstrated impressive mechanical properties (tensile strength: 17.6 ± 0.5 MPa, ductility: 121.8 ± 14.6%, toughness: 17.0 ± 1.6 MJ/m³, Figure S1). These two factors synergistically contribute to a high cohesion performance.

To reveal and prove the underlying mechanism of the proposed adhesion and cohesion interactions hypothesis, we investigated the intermolecular interactions of three distinct scenarios: cellulose-cellulose interaction, DCNRs gel-cellulose interaction, and DCNRs gel-DCNRs gel interaction, using density functional theory (DFT) calculations. Figure 1D plots the differential charge densities (top panel) and hydrogen bonds (bottom panel) in the DFT-optimized molecular structure (unit cell) of each scenario. For instance, in the cellulose-cellulose interaction, hydrogen bonds are established between neighboring -OH groups of cellulose chains, as evidenced by the significantly reduced charge density around the hydrogen atoms of -OH groups (yellow shade) and the increased charge density around the oxygen atoms of -OH groups in the neighboring chain (purple shade). Intriguingly, Figure 1D clearly indicates two intermolecular hydrogen bonds (O3···H6) between the neighboring cellulose chains, as shown by the blue dashed lines. Besides, there exist intramolecular hydrogen bonds (O6···H2) in each molecular chain as well, as illustrated by the orange dashed lines. Intermolecular hydrogen bonds primarily contribute to the strength of the interfacial adhesion. In the DCNRs gel-cellulose interaction, differential charge densities between three pairs of -OH groups (O3···H6, O2···H6, O6···H3) can be found. In other words, the open ring structure in the DCNRs facilitates the formation of additional intermolecular hydrogen bonds. Moreover, the larger shade volume under the same isosurface suggests more electron transfer and stronger hydrogen bonds between the -OH groups of cellulose and DCNRs gel. The synergistic role of quantitative and qualitative enhancement results in stronger adhesion between cellulose and hydrogel-based adhesive. In the DCNRs gel-DCNRs gel interaction, the profiles of the loss and gain of electrons indicate that three pairs of hydrogen bonds (O3···H6, O2···H6, O6···H3) can be formed between neighboring cellulose chains, similar to that in the DCNRs gel-cellulose interaction. However, more electron transfer occurs in the DCNRs gel-DCNRs gel interaction than in the gel-cellulose interaction. It is worth noting that cellulose is the dominant component in wood, and hemicellulose shares similar

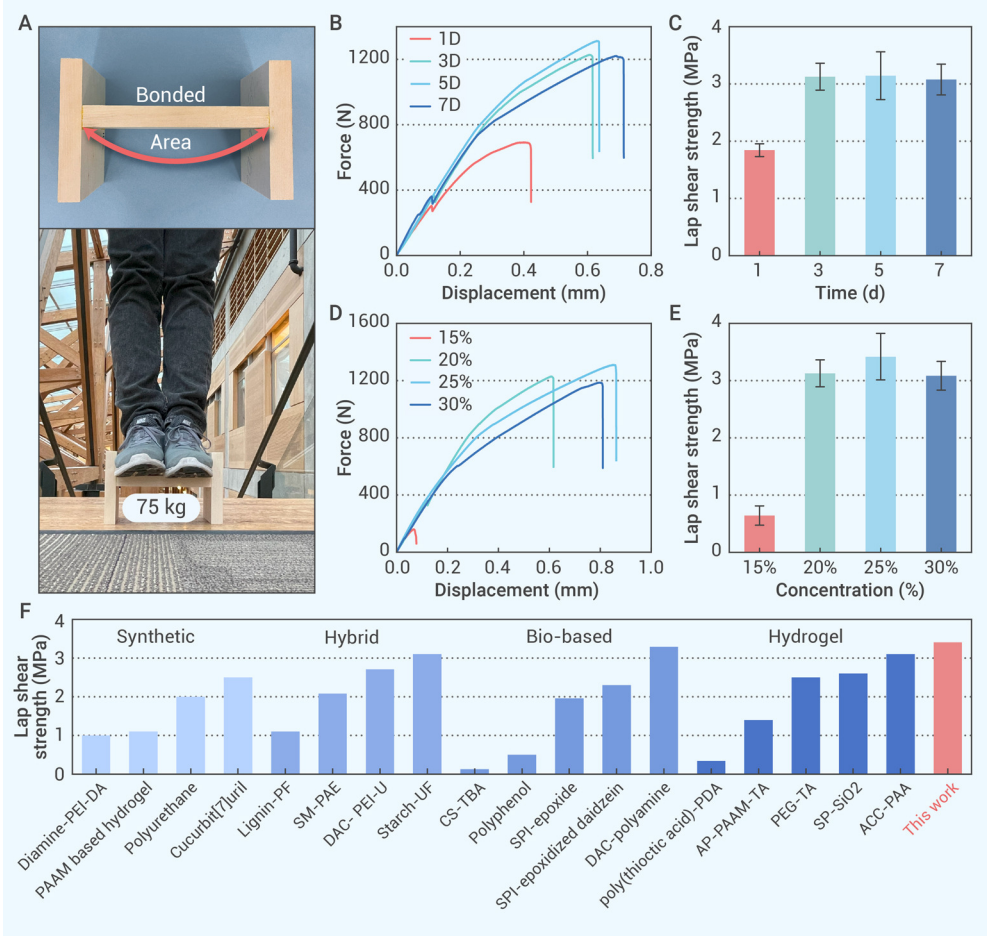

Figure 4. Adhesion of wood (A) The bonded I-beam (solid content: 5.2 mg/cm^2; glued area: ~40 cm^2) can support a human being (75 kg) without failure. (B) Force-displacement curves under different curing times and (C) the corresponding lap shear strength. (D) Force-displacement curves under different DCNRs concentrations and (E) the corresponding lap shear strength. (F) Comparison of the lap shear strength of the DCNRs hydrogel-based adhesive with other adhesives.[1-3, 20, 42-55]

structural units with cellulose; thus, it is reasonable to expect that the adhesion between hydrogel-based adhesive and hemicellulose in wood follows a similar mechanism involving strong binding forces. In addition, due to the high degree of freedom for DCNRs hydrogel, it is also expected that the DCNRs hydrogel can form stronger interactions with the polar functional groups on lignin as compared to cellulose.

Figure 1E plots the side views of the DFT-optimized molecular structures of the three scenarios. In the cellulose-cellulose interaction, the atomic structure of cellulose constrains the degree of freedom of -OH groups so that the hydrogen bonds are formed in the plane. In the DCNRs gel-cellulose interaction, the open hexagon rings in the gel extend out of the plane, enhancing the mobility of -OH groups and the potential to form more out-of-plane hydrogen bonds, as evident in Figure 1D. Notably, more open rings are present in the DCNRs gel-DCNRs gel interaction, which further facilitates the formation of hydrogen bonds and, in turn, strengthens the adhesion. The binding energy between the two molecular chains in the DFT model can be defined as $\Delta E = E_{Total} - E_{Chain1} - E_{Chain2}$, in which E_{Total}, E_{Chain1} and E_{Chain2} represent the total energy of the model system, and the single point energy of individual molecular chains extracted from the total system, respectively. Figure S2 plots the binding energy of the three intermolecular interactions. The cellulose-cellulose interaction has the lowest binding energy (around -1.05 eV), and the DCNRs gel-cellulose binding energy (around -1.32 eV) is comparable to that between DCNRs chains (around -1.33 eV). In other words, by opening the ring structure and converting secondary hydroxyls to primary hydroxyls, stronger intermolecular interactions between the DCNRs chains and cellulose or other DCNRs chains can be expected due to increased hydrogen bond density and van der Waals interactions depending on the specific substrate materials. By enhancing the adhesion and cohesion performances simultaneously, our DCNRs hydrogel-based adhesive exhibits adhesiveness to various substrates (Figure 1F).

Characterizations of DCNRs

After sequential oxidization and reduction, the cellulose pulp was converted to rod-like nanoparticles. Figure 2A shows the digital photos of NBSK pulp suspension, dialdehyde cellulose (DAC) suspension, and DCNRs suspension at 1 wt% concentration. The pulp suspension showed high opaqueness due to the large fiber morphology (Figure S3a). After oxidization, the long cellulose fibers were cleaved into short microfibers (Figure S3b) due to the ring-opening reaction, and the suspension became semi-transparent with slightly increased transmittance compared to the original pulp suspension. However, after reduction, the suspension became highly transparent (nearly 100% transmittance, Figure S4), suggesting the sizes were further reduced. ATR-FTIR was used to indicate the successful transformation from secondary hydroxyl groups to primary hydroxyl groups as displayed in Figure 2B. After the oxidization and reduction process, the absorbance band of C-H stretching at 2926 cm^{-1} and 2883 cm^{-1} in DCNRs became more prominent than in the pulp. In addition, the absorbance assigned to primary OH groups at 1050 cm^{-1} increased while the absorbance assigned to secondary OH groups at 1104 cm^{-1} decreased. Besides, the absorbance at1160 cm^{-1} corresponding to asymmetric C–O–C bonds in the bridge oxygen also decreased. The ^{13}C NMR and ^{1}H NMR spectra of DCNRs are shown in Figures 2C & S5. The four intense peaks of ^{13}C NMR between 60–105 ppm range were assigned to C1, C4 and C5, C2, C3 and C6, respectively, indicating a high ring-opening degree.[46,47] According to titration results of aldehyde content, the total oxidization degree was 70.6%. Therefore, minor cellulose signals have also been observed, which can be ascribed to the remaining unreacted AGU rings.[46,47] Similar to ^{13}C NMR, some small peaks in ^{1}H NMR spectra were also assigned to the remaining cellulose. Solid-state ^{13}C CP-MAS NMR was further conducted on pulp, DAC and DCNRs. As shown in Figure 2D, after periodate oxidization, the resonance at 105 ppm assigned to the C1 decreased significantly, while the hemiacetal signals (90-100 ppm) of DAC emerged. The absence of signals at 160-200 ppm (Figure S6) indicated that aldehyde groups were converted into hemiacetal entities. Notably, the broad hemiacetal signal in the 90-100 ppm regions disappeared after reduction, revealing that they were reduced to primary hydroxyl groups. Also, the signals in the 55-65 ppm region increased while the 70-80 ppm region decreased, due to the shift of secondary hydroxyl groups to primary groups. These NMR and FTIR results verified that the oxidization and reduction process successfully transformed the secondary -OH groups into primary -OH groups in the prepared DCNRs.

The morphologies of DCNRs were observed using TEM and AFM. As shown in Figures 2E & S7, the DCNRs displayed a typical rod-like structure. AFM image in Figure S8 also displayed similar morphologies. Therefore, XRD diffractogram was further employed to observe the crystalline structure. As shown in Figures S9-S10, the original pulp displayed a highly crystalline cellulose I crystal structure, while DAC exhibited a typical amorphous structure due to the high oxidization degree (70.6%). This was ascribed to the periodate oxidization that induced the ring-opening reaction and severely disrupted the cellulose pulp's crystalline structure. Interestingly, after reduction, the dialcohol nanocellulose regained crystalline structure as reflected by

both the XRD diffractogram (Figure S9) and 2D XRD pattern (Figure 2F), which was likely due to the crystallization of stereoregular DCNRs[46] under ambient drying. However, for the freeze-dried dialcohol cellulose, the XRD patterns showed two broad rings, indicating that it was not crystalline (Figure 2F).

Injectability and rheology properties of DCNRs hydrogel

The oxidization-mediated ring-opening process strongly increased the chain flexibility (as revealed by T_g, Figure S11) of DCNRs. Also, the ring-opening reaction induced more intermolecular interactions between DCNRs, which was conducive to the formation of continuous network. Therefore, we speculated that DCNRs hydrogel could be formed with a high concentration of DCNRs. As proof of concept, 2.5 g freeze-dried DCNRs were dispersed in 7.5 g water assisted by sonication and formed a hydrogel with 25 wt.% concentration (H-25%). As shown in Figure 3A, when the glass vial containing H-25% was inverted, the gel maintained at the bottom of the glass vial. Impressively, the prepared gels also exhibited injectability as shown in Figures 3B & S12, which was essential for the application as adhesives. The H-25% hydrogel could be easily extruded from a syringe nozzle and restored viscoelastic gel-like behavior when the applied stress was removed. Letters "UBC" could be easily written through the syringe by hand, indicating the thixotropic behaviors of DCNRs-based hydrogels. Rheological studies were performed to further investigate the dynamic viscoelastic and shear thinning behavior of the formed hydrogels. Firstly, the amplitude sweep measurements were conducted in the range of 0.01-500 Pa and 0.1-100% strain, respectively. As shown in Figure 3C, under small oscillation stress, for H-20%, H-25%, and H-30%, both G' (storage modulus) and G" (loss modulus) were highly stable and constant, and the G' values were larger than G" values, which indicated a typical gel-like behavior. However, for H-15%, the G" values were larger than G' values in the whole stress range, demonstrating a sol-like behavior due to the insufficient interactions. As the oscillation stress increased, the G' and G" values gradually intersected with each other. They exhibited a gel-sol transformation, also revealed by the changes in phase angle (Figure S13). The intersection point was 34 Pa, 251 Pa and 431 Pa for H-20%, H-25%, and H-30%, respectively, suggesting that higher DCNRs concentration can induce more intermolecular interactions to form a more stable structure. For strain sweep experiments, although the G' and G" values showed a similar trend as stress sweep for each group (Figure 3D), the trend for intersection points exhibited a minor difference (9%, 56%, and 36% for H-20%, H-25% and H-30%, respectively). The decreased intersection strain for H-30% was attributed to the stress concentration effect induced by the aggregation formed under high nanoparticle concentration. Frequency sweep tests between 0.1-50 Hz were performed further to evaluate the stability of these hydrogels and the results are shown in Figure 3F. H-30% and H-25% displayed typical gel-like behaviors (G' > G") independent of the frequency range, revealing highly stable structures. However, for H-20%, gel-sol transformation occurred under high frequency owing to insufficient crosslinking. In addition, regarding the injectability, a continuous flow sweep experiment was carried out in the shear rates range of 0.1−10 s^{-1} (Figure 3E). The viscosity of hydrogel decreased significantly when the shear rates increased, showing a typical shear-thinning behavior. The shear stress under continuous flow sweep was shown in Figure S14. It was observed that at various concentrations, the shear stress remained consistently below 500 Pa, which is beneficial for the injectability in various applications.

Adhesion to wood

We further utilized DCNRs hydrogels as wood adhesives. Due to the improved chain flexibility and abundant primary hydroxyl groups, the hydrogel-based adhesives displayed strong adhesion toward basswood. As shown in Figure 4A, three wood panels bonded by H-25% (~900 mg) with a small-bonded area (~20 cm^2) could withstand an adult (75 kg) without failure, demonstrating a highly strong adhesion. Impressively, two wood slides bonded by H-25% (bonded area: ~4 cm^2) could even lift an adult (75 kg), as shown in Figure S15. It should be noted that the adhesion mechanism of this hydrogel-based adhesive is through the loss of water, and the formation of mechanical interlocking and hydrogen bonds. Therefore, no heat or even pressure is needed, making the process much easier and energy efficient. Lap shear tests were employed to quantify the adhesive strength. The lap shear sample was prepared as shown in Figure S16, and then the dry bonding strength was evaluated. Figures 4B-C displayed the effect of curing time on adhesion strength using H-20%. The solid content was fixed as ~4 mg/cm^2 (Figure S17a). As the curing time prolonged, the lap shear strength increased significantly from 1.84 ±0.11 MPa (1 day) to 3.13 ±0.24 MPa (3 days) and then maintained nearly constant for further curing (3.14 ±0.42 MPa for 5 days and 3.07 ±0.27 MPa for 7 days). This suggested that after 3 days of curing, all water in the H-20% between the adherends was removed, forming strong bonds. As shown in digital photos in Figure S18a and microscopy images in Figure S19a, regardless of the curing time, all samples experienced wood failure rather than glue failure, implying that the shear strength of basswood is lower than that of the adhesive. In addition, the influence of DCNRs concentration has also been investigated in Figures 4D-E (corresponding solid content: Figure S17b). As the solid content increased, the lap shear strength firstly increased and then decreased. For H-15%, the liquid-like structure could not maintain the shape integrity of adhesive on wood, and the water was quickly adsorbed by wood, which can lead to a starved glue line. Therefore, sufficient mechanical interlocking could not be formed, which induced a relatively low adhesion strength (0.64 ± 0.17 MPa). The surfaces also indicated insufficient mechanical interlocking after adhesion failure, as shown in Figure S18b & S19b. The H-15% mainly displayed a cohesive failure within the glue. However, for higher concentrations, the hydrogel structure locked the internal water to form sufficient mechanical interlocking, and the high solid content ensured sufficient interface interactions such as abundant hydrogen bonds, thereby demonstrating a strong adhesion, which was superior to many reported adhesives (Figure 4F). To further validate our conclusions, glue lines of DCNRs adhesives with different concentrations were observed by OM (Figures S20a-d). For H-15% adhesive, the glue line displayed an obvious gap between two wood slides. In contrast, for H-20% and H-25%, the glue line suggested that the adhesives gradually penetrated the wood substrates and formed stable and sufficient mechanical interlocking, which can also be confirmed by the wood failure. Besides, Figure S21a showed the cross-section photo of DCNRs hydrogel (dyed with calcofluor white) bonded wood. It is evident that the hydrogel penetrated the wood structure, creating stable mechanical interlocking. Furthermore, we employed confocal microscopy with a 405 nm laser to directly observe this penetration. As shown in Figure S21b, after the curing and drying process, the hydrogel effectively establishes strong interlocking with the substrates depicted by the fluorescent area corresponding to the adhesive that penetrated the wood. Interestingly, after 100 cyclic mechanical loading and unloading tests under 500 N load (Figure S22), the adhesion interface was still bonded closely together, and only a small displacement of ~100 μm was present, indicating that the DCNRs hydrogel-based adhesive can withstand a harsh mechanical fretting operation. The porosity of wood also affected the adhesion strength. As shown in Figure S23, the adhesion strength towards Douglas Fir wood with high density showed a decreased adhesion strength (2.32 ± 0.15 MPa, solid content: 5.45 ± 0.25 mg/cm^2), which can be attributed to the fact that the smaller cells of softwood can prevent the diffusion of the hydrogel into the wood cells, leading to less mechanical interlocking. Conclusively, the high adhesive strength was ascribed to the abundant primary hydroxyl groups, which can induce more hydrogen bonds between DCNRs and wood (Figures 1C-E) and the stable mechanical interlocking formed between adhesive and wood substrates (Figure S21).

Universality of DCNRs hydrogel-based adhesive

For practical applications, hydrogel-based adhesives are supposed to be applicable to various substrates. Therefore, this section examined the universality of DCNRs hydrogel-based adhesive towards different substrates. Figure S24 schematically illustrates the preparation process for adhesives on substrates. Firstly, DCNRs hydrogel-based adhesive was injected onto a piece of a rectangular substrate and formed a hydrogel coating. Then, another piece of the substrate was pressed against the coating area (~4 cm^2). After curing at room temperature for 3 days, the samples were tested through lap shear tests. Figure 1F displayed that the hydrogel-based adhesive could adhere to different solid materials (Teflon, rubber, ceramic, wood, graphite, metal, glass, and plastic), indicating that the adhesive was universal.

Figures S25a & b further displayed the force-displacement curves and lap shear strength towards four typical materials. The adhesion strength was 0.77 ±0.38 MPa, 0.37 ±0.01 MPa, 0.36 ±0.06 MPa, 0.11 ±0.01 MPa for glass, copper, PET, and aluminum, respectively. Compared to wood, the reduced adhesion strength further confirmed that mechanical interlocking is critical in forming strong bonds, and this DCNRs hydrogel-based adhesive is more effective towards hydrophilic porous structures.

CONCLUSION

In summary, we reported a strong hydrogel-based adhesive fabricated from cellulose. The hydrogel consisted of high-concentration DCNRs, prepared by sequentially oxidizing and reducing cellulose. We demonstrated that the secondary hydroxyl groups on AGU rings were successfully converted into primary hydroxyl groups in the oxidization-reduction process. This conversion provided more chain flexibility for DCNRs and enabled the high dispersity of DCNRs in water, thereby inducing the formation of DCNRs hydrogels. A high concentration of DCNRs induced a stable hydrogel structure with excellent injectability, which was essential for on-demand and site-specific adhesives. More importantly, the breakage of the C2-C3 bond liberated the rigid AGU rings and endowed more flexibility and less steric effect for the primary hydroxyl groups. Accordingly, this allowed more intermolecular hydrogen bonds and more out-of-plane hydrogen bonds between DCNRs and cellulose chains at the molecular level, thus resulting in a high adhesion strength towards wood substrates. Besides, the hydrogel-based adhesive demonstrated universality towards various substrates. In summary, this research reveals the potential of a robust DCNRs hydrogel-based adhesive as a sustainable alternative to traditional fossil-based counterparts. It also lays the groundwork for the development of future biomass-based adhesives.

REFERENCES

1. Li, A., Jia, Y., Sun, S., et al. (2018) Mineral-enhanced polyacrylic acid hydrogel as an oyster-inspired organic–inorganic hybrid adhesive. ACS Appl. Mater. Interfaces. **10**: 10471-10479. DOI: 10.1021/acsami.8b01082.
2. Pang, H., Yan, Q., Ma, C., et al. (2021) Polyphenol-metal ion redox-induced gelation system for constructing plant protein adhesives with excellent fluidity and cold-pressing adhesion. ACS Appl. Mater. Interfaces. **13**: 59527-59537. DOI: 10.1021/acsami.1c18401.
3. Choi, Y., Kang, K., Son, D., et al. (2022) Molecular rationale for the design of instantaneous, strain-tolerant polymeric adhesive in a stretchable underwater human–machine interface. ACS Nano **16**: 1368-1380. DOI: 10.1021/acsnano.1c09393.
4. Pei, X., Wang, J., Cong, Y., et al. (2021) Recent progress in polymer hydrogel bioadhesives. J. Polym. Sci. **59**: 1312-1337. DOI: 10.1002/pol.20210249.
5. Zhang, W., Hu, J., Yang, H., et al. (2021). Fatigue-resistant adhesion ii: swell tolerance. extrem. Mech. Lett. **43**: 101182. DOI: 10.1016/j.eml.2021.101182.
6. Zhang, W., Gao, Y., Yang, H., et al. (2020). Fatigue-resistant adhesion I. Long-chain polymers as elastic dissipaters. Extrem. Mech. Lett. **39**: 100813. DOI: 10.1016/j.eml.2020.100813.
7. Sun, J., Tan, H., Liu, H., et al. (2020). A reduced polydopamine nanoparticle-coupled sprayable PEG hydrogel adhesive with anti-infection activity for rapid wound sealing. Biomater. Sci. **8**: 6946–6956. DOI: 10.1039/D0BM01213K.
8. Oelker, A.M., Berlin, J.A., Wathier, M., and Grinstaff, M.W. (2011). Synthesis and characterization of dendron cross-linked peg hydrogels as corneal adhesives. Biomacromolecules **12**: 1658–1665. DOI: 10.1021/bm200039s.
9. Wang, J., Zhang, N., Tan, Y., et al. (2022). Sweat-Resistant Silk Fibroin-Based Double Network Hydrogel Adhesives. ACS Appl. Mater. Interfaces. **14**: 21945–21953. DOI: 10.1021/acsami.2c02534.
10. Yan, Y., Xu, S., Liu, H., et al. (2020). A multi-functional reversible hydrogel adhesive. Colloids Surfaces A Physicochem. Eng. Asp. **593**: 124622. DOI: 10.1016/j.colsurfa.2020.124622.
11. Yuk, H., Varela, C.E., Nabzdyk, C.S., et al. (2019). Dry double-sided tape for adhesion of wet tissues and devices. Nature **575**: 169–174. DOI: 10.1038/s41586-019-1710-5.
12. Joshi, S., Mahadevan, G., Verma, S., and Valiyaveettil, S. (2020). Bioinspired adenine–dopamine immobilized polymer hydrogel adhesives for tissue engineering. Chem. Commun. **56**: 11303–11306. DOI: 10.1039/D0CC04909C.
13. Zhang, J.N., Zhu, H., Liu, T., et al. (2020). Strong adhesion of hydrogels by polyelectrolyte adhesives. Polymer (Guildf). **206**: 122845. DOI: 10.1016/j.polymer.2020.122845.
14. Kim, K., Shin, M., Koh, M., et al. (2015). TAPE : a medical adhesive inspired by a ubiquitous compound in plants. Adv. Func. Mater. **25**: 2402–2410. DOI: 10.1002/adfm.201500034.
15. Chen, K., Lin, Q., Wang, L., et al. (2021). An all-in-one tannic acid-containing hydrogel adhesive with high toughness , notch insensitivity , self-healability , tailorable topography , and strong , instant , and on-demand underwater adhesion. ACS Appl. Mater. Interfaces. **13**: 9748–9761. DOI: 10.1021/acsami.1c00637.
16. Yang, J., Bai, R., and Suo, Z. (2018). Topological adhesion of wet materials. Adv. Mater. **30**: 1800671. DOI: 10.1002/adma.201800671.
17. Hong, S., Pirovich, D., Kilcoyne, A., et al. (2016). Supramolecular metallo-bioadhesive for minimally invasive use. Adv. Mater. **28**: 8675–8680. DOI: 10.1002/adma.201602606.
18. Yuan, J., Du, G., Yang, H., et al. (2022). Functionalization of cellulose with amine group and cross-linked with branched epoxy to construct high-performance wood adhesive. Int. J. Biol. Macromol. **222**: 2719–2728. DOI: 10.1016/j.ijbiomac.2022.10.053.
19. Zhao, D., Zhu, Y., Cheng, W., Xu, G., Wang, Q., Liu, S., Li, J., Chen, C., Yu, H., and Hu, L. (2020). A dynamic gel with reversible and tunable topological networks and performances. Matter **2**: 390–403. DOI: 10.1016/j.matt.2019.10.020.
20. Liu, S., Du, G., Yang, H., et al. (2021). Developing high-performance cellulose-based wood adhesive with a cross-linked network. ACS Sustain. Chem. Eng. **9**: 16849–16861. DOI: 10.1021/acssuschemeng.1c07012.
21. Tardy, B.L., Richardson, J.J., Greca, L.G., et al. (2020). Exploiting supramolecular interactions from polymeric colloids for strong anisotropic adhesion between solid surfaces. Adv. Mater. **32**: 1906886. DOI: 10.1002/adma.201906886.
22. Liu, J., Li, J., Yu, F., et al. (2020). In situ forming hydrogel of natural polysaccharides through Schiff base reaction for soft tissue adhesive and hemostasis. Int. J. Biol. Macromol. **147**: 653–666. DOI: 10.1016/j.ijbiomac.2020.01.005.
23. Zeng, Z., Mo, X., He, C., et al. (2016). An in situ forming tissue adhesive based on poly(ethylene glycol)-dimethacrylate and thiolated chitosan through the Michael reaction. J. Mater. Chem. B **4**: 5585–5592. DOI: 10.1039/C6TB01475E.
24. Wang, J., Wang, L., Wu, C., et al. (2020). Antibacterial zwitterionic polyelectrolyte hydrogel adhesives with adhesion strength mediated by electrostatic mismatch. ACS Appl. Mater. Interfaces. **12**: 46816–46826. DOI: 10.1021/acsami.0c14959.
25. Fan, H., Wang, J., and Jin, Z. (2018). Tough, swelling-resistant, self-healing, and adhesive dual-cross-linked hydrogels based on polymer-tannic acid multiple hydrogen bonds. Macromolecules **51**: 1696–1705. DOI: 10.1021/acs.macromol.7b02653.
26. Wu, J., Zhang, Z., Wu, Z., et al. (2022). Strong and ultra - tough supramolecular hydrogel enabled by strain - induced microphase separation. Adv. Funct. Mater. **33**: 2210395. DOI: 10.1002/adfm.202210395.
27. Liu, H., Hu, X., Li, W., et al. (2023). A highly-stretchable and adhesive hydrogel for noninvasive joint wound closure driven by hydrogen bonds. Chem. Eng. J. **452**: 139368. DOI: 10.1016/j.cej.2022.139368.
28. Zhao, X., Liang, Y., Huang, Y., et al. (2020). Physical double-network hydrogel adhesives with rapid shape adaptability, fast self-healing, antioxidant and NIR/pH stimulus-responsiveness for multidrug-resistant bacterial infection and removable wound dressing. Adv. Funct. Mater. **30**: 1910748. DOI: 10.1002/adfm.201910748.
29. Chen, J., Wang, D., Wang, L.H., et al. (2020). An adhesive hydrogel with "load-sharing" effect as tissue bandages for drug and cell delivery. Adv. Mater. **32**: 2001628. DOI: 10.1002/adma.202001628.
30. Zhao, D., Pang, B., Zhu, Y., et al. (2022). A stiffness-switchable, biomimetic smart material enabled by supramolecular reconfiguration. Adv. Mater. **34**: 2107857. DOI: 10.1002/adma.202107857.
31. Zhu, Y., Guo, Y., Cao, K., et al. (2023). A general strategy for synthesizing biomacromolecular ionogel membranes via solvent-induced self-assembly. Nat. Synth. **2**: 864–872. DOI: 10.1038/s44160-023-00315-5.
32. Ng, H.M., Sin, L.T., Bee, S.T., et al. (2017). Review of nanocellulose polymer composite characteristics and challenges. Polym. - Plast. Technol. Eng. **56**: 687–731. DOI: 10.1080/03602559.2016.1233277.
33. Thomas, B., Raj, M.C., Athira, B.K., et al. (2018). Nanocellulose, a versatile green platform: from biosources to materials and their applications. Chem. Rev. **118**: 11575–11625. DOI: 10.1021/acs.chemrev.7b00627.
34. Kresse G, Furthmüller J. (1996) Efficiency of ab-initio total energy calculations for metals and semiconductors using a plane-wave basis set. Comput. Mater. Sci. 6: 15-50. DOI: 10.1016/0927-0256(96)00008-0.
35. Kresse, G. and Furthmüller, J. (1996). Efficient iterative schemes for ab initio total-energy calculations using a plane-wave basis set. Phys. Rev. B 54: 11169. DOI: 10.1103/PhysRevB.54.11169.
36. Blöchl, P. E. (1994). Projector augmented-wave method. Phys. Rev. B 50: 17953. DOI: 10.1103/PhysRevB.50.17953.
37. Perdew, J. P., Burke, K., and Ernzerhof, M. (1996). Generalized gradient approximation made simple. Phys. Rev. lett. 77: 3865. DOI: 10.1103/PhysRevLett.77.3865.
38. Monkhorst, H. J. and Pack, J. D. (1976). Special points for Brillouin-zone integrations. Phys. Rev. B 13: 5188. DOI: 10.1103/PhysRevB.13.5188. DOI: 10.1103/PhysRevB.13.5188.
39. Allouche, A. R. (2011). Gabedit —A graphical user interface for computational chemistry softwares. J. Comput. Chem. 32: 174-182. DOI: 10.1002/jcc.21600. DOI: 10.1002/jcc.21600.
40. Merindol, R., Diabang, S., Mujica, R., et al. (2020). Assembly of anisotropic nanocellulose films stronger than the original tree. ACS Nano **14**: 16525–16534.. DOI: 10.1021/acsnano.0c01372.

41. Li, K., Skolrood, L.N., Aytug, T., et al. (2019). Strong and tough cellulose nanofibrils composite films: mechanism of synergetic effect of hydrogen bonds and ionic interactions. ACS Sustain. Chem. Eng. **7**: 14341–14346. DOI: 10.1021/acssuschemeng.9b03442.
42. Jiang, G., Wang, G., Zhu, Y., et al. (2022). A scalable bacterial cellulose ionogel for multisensory electronic skin. Research **2022**: 9814767. DOI: 10.34133/2022/9814767.
43. Huang, J., Yu, L., Wang, S., et al. (2023). An ultrathin nanocellulosic ion redistributor for long-life zinc anode. Innov. Mater. **1**: 100029. DOI: 10.59717/j.xinn-mater.2023.100029.
44. Sun, X., Zhu, Y., Yu, Z., et al. (2023). Dialcohol cellulose nanocrystals enhanced polymerizable deep eutectic solvent-based self-healing ion conductors with ultra-stretchability and sensitivity. Adv. Sens. Res. **2**: 2200045. DOI: 10.1002/adsr.202200045.
45. Kristiansen, K.A., Potthast, A., Christensen, B.E. (2010) Periodate oxidation of polysaccharides for modification of chemical and physical properties. Carbohydr. Res. **345**: 1264. DOI: 10.1016/j.carres.2010.02.011.
46. Casu, B., Naggi, A., Torri, G., et al. (1985). Stereoregular acyclic polyalcohols and polyacetates from cellulose and amylose. Macromolecules **18**: 2762–2767. DOI: 10.1021/ma00154a068.
47. Painter, T.J. (1988). Control of depolymerisation during the preparation of reduced dialdehyde cellulose. Carbohydr. Res. **179**: 259–268. DOI: 10.1016/0008-6215(88)84123-5.
48. Liu, C., Xie, X., Kong, X., et al. (2022) A removable, antibacterial and strong adhesive based on hyperbranched catechol polymers. Mater. Lett. **316**: 132019. DOI: 10.1016/j.matlet.2022.132019.
49. Borrero-López, A.M., Guzmán, D.B., González-Delgado, J.A., et al. (2021) Toward UV-triggered curing of solvent-free polyurethane adhesives based on castor oil. ACS Sustain. Chem. Eng, **9**: 11032-11040. DOI: 10.1021/acssuschemeng.1c02461.
50. Liu, J., Scherman, O.A. (2018) Cucurbit [n] uril supramolecular hydrogel networks as tough and healable adhesives. Adv. Funct. Mater. **28**: 1800848. DOI: 10.1002/adfm.201800848.
51. Xu, C., Xu, Y., Chen, M., et al. (2020) Soy protein adhesive with bio-based epoxidized daidzein for high strength and mildew resistance. Chem. Eng. J. **390**: 124622. DOI: 10.1016/j.cej.2020.124622.
52. Pan, F., Ye, S., Wang, R., et al. (2020) Hydrogel networks as underwater contact adhesives for different surfaces. Mater. Horizons **7**: 2063-2070. DOI: 10.1039/D0MH00176G.
53. Islam, M.N., Faruk, M.O., Rana, M.N., et al. (2021) Preparation and evaluation of rice bran - modified urea formaldehyde as environmental friendly wood adhesive. Glob. Challenges **5**: 2000044. DOI: 10.1002/gch2.202000044.
54. He, X., Liu, R., Liu, H., et al. (2021) Facile preparation of tunicate-inspired chitosan hydrogel adhesive with self-healing and antibacterial properties. Polymers **13**: 4322. DOI: 10.3390/polym13244322.
55. Li, Z., Du, G., Yang, H., et al. (2022) Construction of a cellulose-based high-performance adhesive with a crosslinking structure bridged by Schiff base and ureido groups. Int. J. Biol. Macromol. **223**: 971. DOI: 10.1016/j.ijbiomac.2022.11.069.
56. Huang, X., Chen, Y., Li, J., et al. (2022) Improving the coating and prepressing properties of soybean meal adhesive by constructing a biomimetic topological structure. Mater. Des. **223**: 111163. DOI: 10.1016/j.matdes.2022.111163.
57. Zhang, X., Xu, C., Liu, Z., et al. (2022) A water-resistant and mildewproof soy protein adhesive enhanced by epoxidized xylitol. Ind. Crops Prod. **180**: 114794. DOI: 10.1016/j.indcrop.2022.114794.
58. Huang, C., Peng, Z., Li, J., et al. (2022) Unlocking the role of lignin for preparing the lignin-based wood adhesive: A review. Ind. Crops Prod. **187**: 115388. DOI: 10.1016/j.indcrop.2022.115388.
59. Xu, Y., Zhang, X., Liu, Z., et al. (2022) Constructing SiO_2 nanohybrid to develop a strong soy protein adhesive with excellent flame-retardant and coating ability. Chem. Eng. J. **446**: 137065. DOI: 10.1016/j.cej.2022.137065.
60. Zhang, H., Xiao, Y., Chen, P., et al. (2022) Robust natural polyphenolic adhesives against various harsh environments. Biomacromolecules **23**: 3493-3504. DOI: 10.1021/acs.biomac.2c00704.
61. Chai, C., Guo, Y., Huang, Z., et al. (2020) Antiswelling and durable adhesion biodegradable hydrogels for tissue repairs and strain sensors. Langmuir **36**: 10448. DOI: 10.1021/acs.langmuir.0c01605.

FUNDING AND ACKNOWLEDGMENTS

Feng Jiang acknowledges the financial support from the Canada Research Chairs program (231928), the Natural Sciences and Engineering Research Council of Canada (NSERC, RGPIN-2018-06818), and the Canada Foundation for Innovation —John R. Evans Leaders Fund (CFI-JELF #37517). Xia Sun acknowledges the Four-Year Fellowship (4YF) from UBC and Paul Heller Memorial Fellowship in Forestry for financial support. The authors acknowledge Yuki Liang for the data acquisition of 13C CP-MAS NMR results and Yoshiharu Nishiyama for the data acquisition of 2D XRD patterns. ZP and TL acknowledge the support of the National Science Foundation, USA (Grants CMMI # 1936452) and the University of Maryland supercomputing resources (http://hpcc.umd.edu) and Maryland Advanced Research Computing Center (MARCC) made available for conducting the research reported in this paper. The funders had no role in study design, data collection and analysis, decision to publish or preparation of the manuscript.

AUTHOR CONTRIBUTIONS

S.X. and P.Z. contributed equally to this work. J.F. and S.X. conceived the concept and designed the experiments. J.F. and L.T. supervised the work. S.X. carried out most experiments and characterizations. P.Z. carried out the computational simulation and analyzed the results. L.L. and R.S. contributed to the NMR experiments. Z.Y., Y.Z. and Y.P. contributed to the characterizations. S.X., P.Z. and J.F. analyzed the data and co-wrote the manuscript. S.X., P.Z., L.T. and J.F. revised the manuscript. All authors commented on the submitted version of the manuscript.

DECLARATION OF INTERESTS

Feng Jiang is an Editorial Board member of The Innovation Materials and was blinded from reviewing or making final decisions on the manuscript. Peer review was handled independently of this member and their research group. The other authors declare no conflicts of interest.

DATA AND CODE AVAILABILITY

The data that support the findings of this study are available from the corresponding author upon reasonable request.

SUPPLEMENTAL INFORMATION

It can be found online at https://doi.org/10.59717/j.xinn-mater.2023.100040

LEAD CONTACT WEBSITE

https://nanocellulose.forestry.ubc.ca/